On the Dynamics of Errors in Finite-Difference Approximations for Wave Equations

David J. Muraki

Department of Mathematics, Simon Fraser University, Burnaby BC, Canada, V5A 1S6

Abstract

Exact numerical Green's functions are derived for semi-discrete wave equations for various finite-difference approximations of the spatial derivative. The asymptotic method of steepest descent is used to analyze resolution errors for finite spatial-discretization. For discretizations of the one-way wave equation, the space-time location of dispersive wave errors from Gaussian initial conditions is shown to have a self-similar behavior with spatial resolution. A type of exponentially-small aliasing error is identified by the asymptotic method of steepest descent.

Key words:
semi-discretized PDEs, finite-difference errors, numerical Green's functions, method of steepest descent.

1. Introduction

Of the various approaches to the numerical approximation of differential equations, methods involving finite-differences were among the first to be implemented and analyzed [1]. As an essential part of the basic canon of numerical analysis, the basics of finite-difference methods are well laid out in the standard textbooks [2, 3, 4, 5, 6]. Of critical importance are the issues of accuracy and stability, especially their scaling behavior with decreasing discretization stepsize. However, as the equations of finite-difference approximations are themselves descriptions of a dynamical system, their own properties can also be studied — in particular, as being representative of observed behavior in computational implementations.

Two often cited perspectives on the dynamics of equations for finite-difference approximations are the modified equation analysis, as developed by Warming and Hyatt [7]; and the group velocity analysis, as presented by Trefethen [8]. A common feature of both approaches is the characterization of the behavior of errors that arise due to the finite, albeit small, discretization of the numerical approximation. In this note, we present ideas along these lines that have been inspired by some little-known works of Pearson [9, 10], that quantify the dynamics of approximate equations with finite-discretization. The first results are the presentation of a family of exact numerical Green's functions for various semi-discrete (continuous in time, finite-difference in space) approximations. These solutions include those described in the original works of Pearson, and more generally, add to the thorough discussion for semi-discrete approximations found in the survey of Vichnevetsky and Bowles [11]. As initial value Green's functions, the behavior of these solutions encapsulates the essential dynamics of the underlying approximation, and as envisioned by Pearson, provides a starting point for the discussion of resolution errors for finite-differences. The second results are an application of the asymptotic method of steepest descent to identify and quantify dispersive resolution errors that are inherent in finite-difference approximations. A testcase for understanding the appearance of resolution errors specializes the integral asymptotics of Pearson to Gaussian initial conditions of varying breadth. Based on Fourier transforms, this direction of thinking builds strongly upon the ideas of group velocity, and the Fourier approach developed in [11].

2. Exact Semi-Discrete Green's Functions

A common introductory context for the numerical approximation of hyperbolic wave systems begins from a discussion of the one-way wave equation, $u_t + cu_x = 0$ with constant, right-going wavespeed $c > 0$ [2, 6]. Consider then,

a semi-discretized (SD) version of the linear, one-way wave equation

$$\frac{\partial u}{\partial t}(x,t) + c\ \frac{u(x+\Delta x,t) - u(x-\Delta x,t)}{2\Delta x} = 0 \tag{1}$$

where the spatial derivative is approximated by a centered finite-difference. As the finite-differencing restricts the spatial coupling to intervals of Δx, it is typical for numerical methods to focus attention on discrete gridpoint values at $x_n = n\Delta x$ with indexing on integers n. But this restriction to the lattice is not necessary, and finite-difference equations like (1) can equally well be considered with an initial condition $u(x,0) = U(x)$ specified on the whole real axis, $-\infty < x < +\infty$, And although spatial coupling remains restricted to Δx-lattices, the behaviors of (1) can nonetheless be understood using methods of continuous analysis. For instance, considering solutions having the Fourier form, $e^{i(kx-\omega t)}$, leads to the semi-discrete dispersion relation

$$\omega(k) = \frac{c}{\Delta x}\ \sin k\Delta x \tag{2}$$

where k is a real-valued wavenumber. In the continuum limit $\Delta x \to 0$, the exact dispersionless relation $\omega = ck$ is recovered; while for finite Δx, the analysis of this numerical dispersion relation leads to familiar discussion of phase and amplification errors [2, 3].

However, as the difference equation (1) is linear, more general solutions are obtained through superimposition of these exponential modes (2) by Fourier integration over the wavenumber. The Fourier integral

$$\mathcal{G}(x,t) = \frac{1}{2\pi}\int_{-\infty}^{+\infty} e^{ikx}\ \exp\left(-i\ \frac{ct}{\Delta x}\sin k\Delta x\right) dk \tag{3}$$

represents a solution that is the initial value Green's function for (1) since $\mathcal{G}(x,0) = \delta(x)$. By (2), the time-exponential factor, $e^{-i\omega(k)t}$, is a periodic function of the wavenumber k, and thus, is expressible as a Fourier series

$$\exp\left(-i\ \frac{ct}{\Delta x}\sin k\Delta x\right) = \sum_{n=-\infty}^{+\infty} g_n(t)\ e^{-in\,k\Delta x}\ . \tag{4}$$

This periodicity in wavenumber (with period $2\pi/\Delta x$) is a direct result of aliasing on the Δx-grid inherent in the discretization of (1). Pearson noted that this exponential expression is related to the generating function for the Bessel functions ([12], eq 9.1.41) so that the Fourier coefficients are

$$g_n(t) = J_n\left(\frac{ct}{\Delta x}\right) \tag{5}$$

where a typo of a factor of 2 has been corrected from [10]. The Fourier integral (3) is thus a sum of weighted delta functions at the gridpoints $x_n = n\Delta x$,

$$\mathcal{G}(x,t) = \sum_{n=-\infty}^{+\infty} J_n\left(\frac{ct}{\Delta x}\right)\ \delta(x-x_n)\ , \tag{6}$$

where the Bessel functions having negative indices follow the convention $J_{-n}(z) = (-1)^n\, J_n(z)$. Since $\mathcal{G}(x,t)$ is the Green's function for (1), the weights $g_n(t)$ (5) must be an exact formula for the numerical SD Green's function that solves the coupled ODEs

$$g_n' + c\ \frac{g_{n+1} - g_{n-1}}{2\Delta x} = 0 \quad ; \quad g_n(0) = \begin{cases} 1 & \text{for } n = 0 \\ 0 & \text{otherwise} \end{cases}\ . \tag{7}$$

Typical solutions are illustrated in Figure 1 by the grid values, $g_n(t)$ for $\Delta x = 1/4$ at two times, $ct = 2$ and 8.

Following [8], group velocity considerations based on (2) indicates (energy) propagation at all speeds between $\pm c$. Nonetheless, it is still a mildly surprising feature of the SD Green's functions (6), as seen in Figure 1, that the forward time evolution produces visible oscillations that extend fully across the interval $-ct < x < +ct$. The extent of the

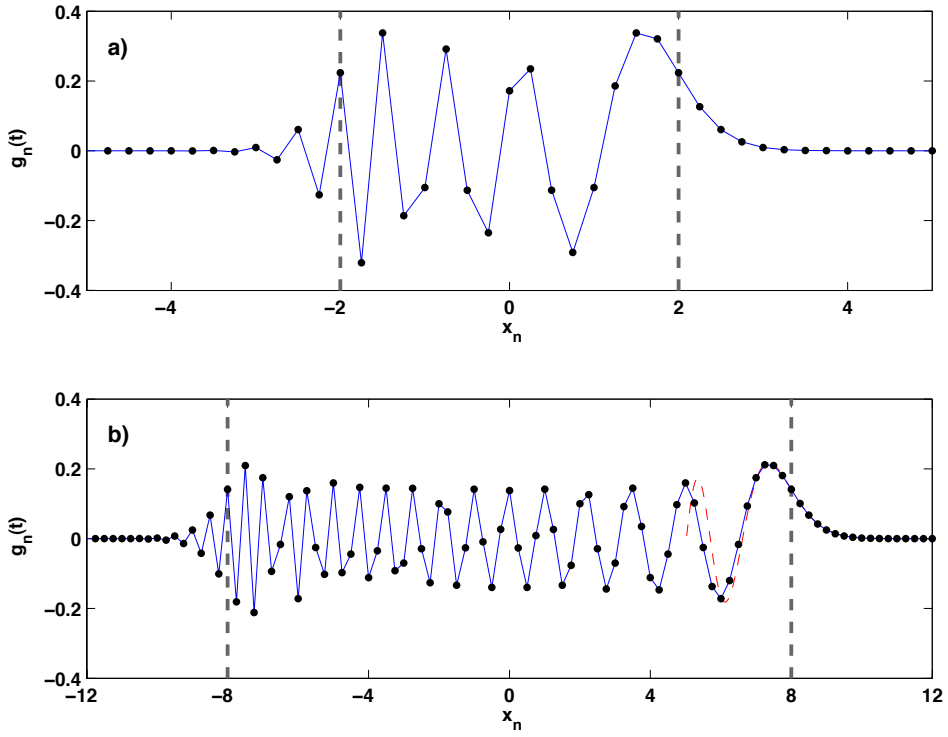

Figure 1: The semi-discrete Green's function, $g_n(t)$, for the one-way wave equation (5) for $\Delta x = 1/4$ at two times: a) $ct = 2$ and b) $ct = 8$. The gray dashed lines demarcate the group velocity region $|x| < ct$. The thin connecting line serves only to highlight the oscillations which tend to grid-scale towards the trailing edge. The dashed curve in b) illustrates the turning point precursor (8) at the leading edge.

group velocity region $|x| < ct$ is indicated by the gray dashed vertical lines in the panels of Figure 1. At the rightward end, is the leading-edge precursor for which (6) has the asymptotic expression

$$g_n(t) \sim \left(\frac{2}{n}\right)^{1/3} \mathrm{Ai}\left(2^{1/3} n^{2/3} \left\{1 - \frac{ct}{x_n}\right\}\right) \tag{8}$$

where n is large, and valid for $x_n - ct = O(n^{1/3}\Delta x)$. Shown as the dashed curve in Figure 1b, this precursor (8) was identified in [10], and follows from the Bessel function (5) limit of large-argument and large-index ([12], eq 10.4.32). The oscillatory tail on the left is created by the emergence of dispersive waves whose group velocities are slower than the characteristic speed, and is exactly as described in [8]. That the trailing tail has the symmetric amplitude structure, but with a grid-scale oscillation follows from the space-time reflection formulas

$$g_{-n}(t) = g_n(-t) = (-1)^n \, J_n\!\left(\frac{ct}{\Delta x}\right) . \tag{9}$$

This reverse propagation of grid-scale oscillations (at wavenumber $k = \pi/\Delta x$) is consistent with group velocity considerations [8][1]. This spatial symmetry in amplitude means that the continuous Green's function $\delta(x - ct)$ cannot emerge as the $\Delta x \to 0$ semi-discrete limit of $\mathcal{G}(x, t)$. Nonetheless, it must be the case that the general solution of the initial value problem for (1) on the infinite line

$$u(x, t) = (\mathcal{G} * U)(x, t) \equiv \int_{-\infty}^{+\infty} \mathcal{G}(x - y, t)\, U(y)\, dy \tag{10}$$

[1] An elegant dynamical explanation for why the one-wave SD wave has two-way propagation is found in Section 6.5 of [11].

must converge to rightward characteristic propagation. Hence, numerical convergence of the SD scheme (1) reduces to understanding the limiting behavior of the above convolution, whose kernel function is increasingly oscillatory as $\Delta x \to 0$. Particularly, the mathematical question of numerical resolution for finite Δx is equivalent to determining the extent to which the limit $u(x,t) \to U(x-ct)$ is being realized *in the sense of distributions*. The 1988 paper of Pearson [10] invoked a tendency to cancellation by the grid-scale oscillations (9), and a further asymptotic analysis of this resolution issue is the subject of Section 3.

The remainder of this Section presents other SD schemes that are solvable by this way of thinking. A summary of discretizations and their exact SD Green's functions is shown in Table 1 The generic form of the SD Green's function is

$$\sum_{n=-\infty}^{+\infty} c_n(t)\ \delta(x-x_n) \tag{11}$$

where the weights $c_n(t)$ are as listed in the fourth column.

2.1. The Diffusion Equation

Consider next, the SD version of the diffusion equation, $u_t = \nu u_{xx}$ based upon a centered-difference approximation of the second derivative in space

$$\frac{\partial}{\partial t}u(x,t) = \nu\ \frac{u(x+\Delta x,t) - 2u(x,t) + u(x-\Delta x,t)}{\Delta x^2} \tag{12}$$

with diffusion coefficient $\nu > 0$. As done similarly for the one-way wave equation, the initial value Green's function is constructed by the Fourier integral

$$\mathcal{H}(x,t) = \frac{1}{2\pi}\int_{-\infty}^{+\infty} e^{ikx}\ \exp\left(\frac{2\nu t}{\Delta x^2}\ (\cos k\Delta x - 1)\right) dk\ . \tag{13}$$

This can be re-expressed as a delta series using the generating function of the modified Bessel function ([12], eq 9.6.33), and gives the Green's function weights for the series form (11)

$$h_n(t) = \exp\left(-\frac{2\nu t}{\Delta x^2}\right)\ I_n\left(\frac{2\nu t}{\Delta x^2}\right)\ . \tag{14}$$

For positive diffusion coefficient, $\nu > 0$, the exponential decay exactly counteracts the growth of the modified Bessel function, and the SD Green's function approximates well the Gaussian profile of the continuous diffusion Green's function when $\nu t \gg \Delta x^2$

$$h_n(t) \sim \frac{\Delta x}{\sqrt{4\pi\nu t}}\ \exp\left(-\frac{x_n^2}{4\nu t}\right)\ . \tag{15}$$

Note the above includes an additional scaling of Δx accounting for the delta functions in the series (11). The dashed curve in Figure 2 illustrates this comparison of the (scaled) continuous Gaussian to the SD values (14) at time $\nu t = 1/4$ with a grid-spacing of $\Delta x = 1/4$, and suggests pointwise convergence of the $\Delta x \to 0$ limit. For backward diffusion, the formula (14) can be modified either by taking $\nu < 0$, or reversing time. In the latter case, it then follows that Green's function weights for unstable diffusion (and $\nu > 0$) are

$$h_n(-t) = \exp\left(\frac{4\nu t}{\Delta x^2}\right)\ (-1)^n\ h_n(t)\ . \tag{16}$$

The numerical effects of the discrete backward diffusion are thus succinctly expressed as the destabilization of forward diffusion by exponential growth with a grid-scale oscillation.

2.2. The Free-Space Schrödinger Equation

The free-space Schrödinger equation is obtained when the diffusion constant in (12) is replaced by the pure imaginary quantity, $\nu = i\tilde{\nu}$. The identity connecting Bessel functions for imaginary argument $I_n(z) = (-i)^n J_n(iz)$ ([12], eqn 9.6.3) provides modification to complex-valued weights

$$\tilde{h}_n(t) = i^n \exp\left(-i\,\frac{2\tilde{\nu}t}{\Delta x^2}\right)\ J_n\left(\frac{2\tilde{\nu}t}{\Delta x^2}\right)\ . \tag{17}$$

This solution features significant grid-scale oscillations everywhere along the x-axis grid.

PDE	differencing	SD equation	SD Green's function weights, $c_n(t)$
one-way wave	centered	$\frac{\partial u}{\partial t}(x,t) + c\,\frac{u(x+\Delta x,t) - u(x-\Delta x,t)}{2\Delta x} = 0$	$g_n(t) = J_n\left(\frac{ct}{\Delta x}\right)$
forward diffusion	centered	$\frac{\partial}{\partial t}u(x,t) = \nu\,\frac{u(x+\Delta x,t) - 2u(x,t) + u(x-\Delta x,t)}{\Delta x^2}$	$h_n(t) = \exp\left(-\frac{2\nu t}{\Delta x^2}\right) I_n\left(\frac{2\nu t}{\Delta x^2}\right)$
backward diffusion	centered	forward diffusion, with time reversed	$h_n(-t) = (-1)^n\,\exp\left(\frac{4\nu t}{\Delta x^2}\right) h_n(t)$
free-space Schrödinger	centered	$\frac{\partial}{\partial t}u(x,t) = -i\tilde{\nu}\,\frac{u(x+\Delta x,t) - 2u(x,t) + u(x-\Delta x,t)}{\Delta x^2}$	$\tilde{h}_n(t) = i^n\,\exp\left(-i\,\frac{2\tilde{\nu}t}{\Delta x^2}\right) J_n\left(\frac{2\tilde{\nu}t}{\Delta x^2}\right)$
one-way wave	upwind*	$\frac{\partial u}{\partial t}(x,t) + c\,\frac{u(x,t) - u(x-\Delta x,t)}{\Delta x} = 0$	$g_n^+(t) = (h * g)_n(t) = \sum_{k=-\infty}^{+\infty} h_{n-k}(t)\,g_k(t)$
one-way wave	downwind*	$\frac{\partial u}{\partial t}(x,t) + c\,\frac{u(x+\Delta x,t) - u(x,t)}{\Delta x} = 0$	$g_n^-(t) = (-1)^n\,\exp\left(\frac{4\nu t}{\Delta x^2}\right) g_n^+(-t)$
two-way wave	centered	$\frac{\partial^2 u}{\partial t^2}(x,t) - c^2\,\frac{u(x+\Delta x,t) - 2u(x,t) + u(x-\Delta x,t)}{\Delta x^2} = 0$	$w_n^a(t) = J_{2n}\left(\frac{2ct}{\Delta x}\right)$ $w_n^b(t) = -\frac{n\Delta x}{ct}\,J_{2n}\left(\frac{2ct}{\Delta x}\right)$

Table 1: A summary of exact formulas for SD Green's functions as in (6). The coefficients are assumed positive ($c > 0$, $\nu > 0$), and for the upwind* and downwind* SD Green's functions, the diffusion coefficient takes the specific value $\nu = c\Delta x/2$. The Green's functions are initially zero at all gridpoints and normalized to one at $x_0 = 0$; the exception is the second of the two-way wave solutions where $w_n^b(t)$ satisfies the derivative initial value (26).

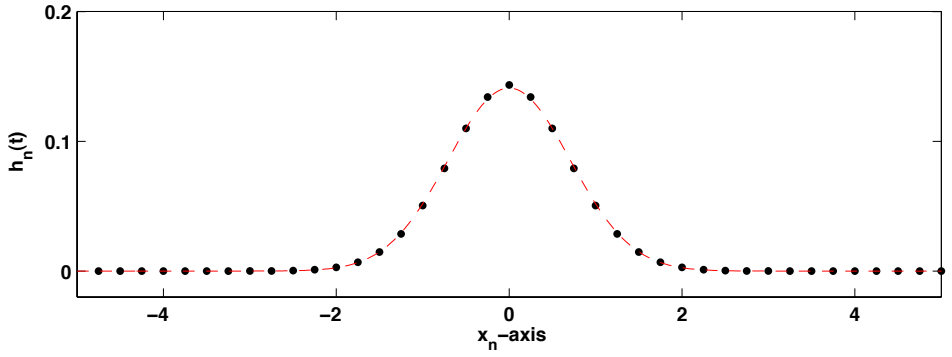

Figure 2: The semi-discrete Green's function, $h_n(t)$, for the diffusion equation (14) for $\Delta x = 1/4$ at time $\nu t = 1/4$. For comparison, the dashed curve is the (scaled) continuous Green's function (15), and suggests pointwise convergence.

2.3. One-Sided Differences

One of the primary lessons in the numerical analysis of finite-differencing is the stability dichotomy between the asymmetric schemes of upwind and downwind differencing for wave equations. The upwind scheme for the one-way wave, as written in Table 1 for $c > 0$, has the complex-valued SD dispersion relation

$$\omega(k) = -i\,\frac{c}{\Delta x}\left(1 - e^{-ik\Delta x}\right) = \frac{c}{\Delta x}\,\left(\sin k\Delta x - i\,\left(1 - \cos k\Delta x\right)\right)\ . \tag{18}$$

The real part is exactly the centered-difference result (2), while the imaginary part is the SD diffusion decay rate as in (13) with $\nu = c\Delta x/2$. Since the dispersion relation is a sum of propagation and diffusion, the Fourier construction analogous to (3) and (13) leads to an exact formula for upwind weights expressed as a discrete convolution

$$g_n^+(t) = (h * g)_n(t) = \sum_{k=-\infty}^{+\infty} h_{n-k}(t)\, g_k(t) \tag{19}$$

where the $g_n(t)$ and $h_n(t)$ are identical to those previously obtained as (5) and (14). Thus, the weights for the upwind SD Green's function, $g_n^+(t)$, are simply a composition of the combined effects of centered-difference propagation and diffusion (with Δx-dependent coefficient, $\nu = c\Delta x/2$). Figure 3 provides a direct comparison of the upwind SD Green's function to the oscillatory centered-difference version of Figure 1a ($\Delta x = 1/4$ and $ct = 2$). For this illustration, the diffusion weights involved in the convolution (19) at $ct = 2$ are precisely those chosen for the example of Figure 2. It is apparent from Figure 3 that the smoothing effects of the diffusion have completely overcome the oscillations of the centered-difference propagation in the convolution. This non-negativity of the Green's function weights reflects the monotone property of the SD upwind scheme, as can be inferred from the quadrature formula

$$u_n(t) = u_n(0)\, e^{-ct/\Delta x} + \int_{-\infty}^{t} u_{n-1}(s)\, e^{-c(t-s)/\Delta x}\, ds\ . \tag{20}$$

that solves the one-sided version of the ODE system (7). Finally, it is well-known that the downwind scheme for the one-way wave generates an unstable numerical method. The weights for the downwind scheme, $g_n^-(t)$, are obtained from (19) by time-reversing the diffusion part. Manipulation of the convolution using (9) and (16) gives

$$g_n^-(t) = \exp\left(\frac{4\nu t}{\Delta x^2}\right)\,(-1)^n\, g_n^+(-t) \tag{21}$$

which shows that not only is the downwind SD Green's function growing exponentially with a grid-scale oscillation, it is also propagating in the reverse direction.

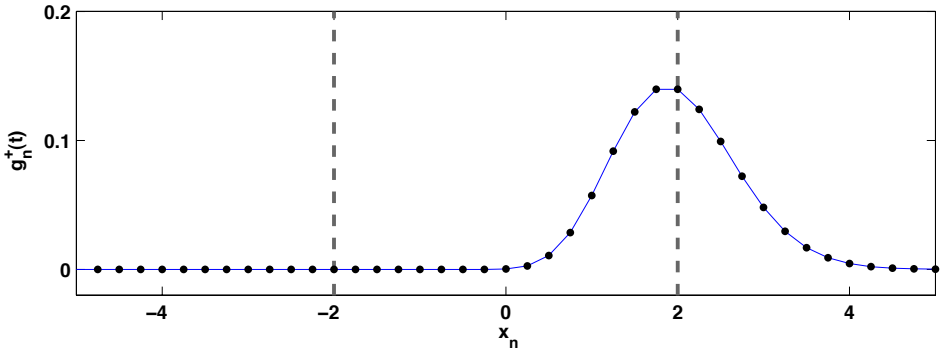

Figure 3: The semi-discrete Green's function, $g_n^+(t) = (h * g)_n(t)$, for the upwind discretization with $\Delta x = 1/4$ at time $ct = 2$. The gray dashed lines demarcate the group velocity region $|x| < ct$. The thin line serves only to connect the discrete values. The numerical diffusion coefficient, $\nu = c\Delta x/2$, is the same as that chosen for Figure 2. In sharp contrast with Figure 1a, the Green's function for the monotone upwind scheme has no numerical oscillation.

2.4. The Wave Equation

Consider the SD version of the wave equation, $u_{tt} - c^2 u_{xx} = 0$, with centered-differencing in space as shown in Table 1[2]. It has a double-valued SD dispersion relation

$$\omega(k) = \pm \frac{2c}{\Delta x} \sin\left(\frac{k\Delta x}{2}\right) \tag{22}$$

which derives from a perfect square formed from a half-angle trig identity. By construction, the Fourier integral

$$\mathcal{W}^a(x,t) = \frac{1}{2\pi}\int_{-\infty}^{+\infty} e^{ikx} \cos\left(\frac{2ct}{\Delta x} \sin\left(\frac{k\Delta x}{2}\right)\right) dk \tag{23}$$

corresponds to the initial value Green's function with $\mathcal{W}^a(x,0) = \delta(x)$ and $\mathcal{W}_t^a(x,0) = 0$. Another Bessel generating function ([12], eq 9.1.42) produces an exact formula for series weights

$$w_n^a(t) = J_{2n}\left(\frac{2ct}{\Delta x}\right) . \tag{24}$$

The nature of two-way propagation is closely related to the one-way wave, as the weights, $w_n^a(t)$, are precisely the even index values of (5) with the discretization Δx halved (see also [11], sect 2.9). This relationship is clearly illustrated by the comparison of (24) plotted in Figure 4a for $\Delta x = 1/2$ and $ct = 2$, with the even index values shown in Figure 1b. A second, linearly-independent solution is given by

$$\mathcal{W}^b(x,t) = \frac{i}{2\pi}\int_{-\infty}^{+\infty} e^{ikx} \cos\left(\frac{k\Delta x}{2}\right) \sin\left(\frac{2ct}{\Delta x} \sin\left(\frac{k\Delta x}{2}\right)\right) dk \tag{25}$$

and corresponds to initial values $\mathcal{W}^b(x,0) = 0$ with

$$\mathcal{W}_t^b(x,0) = -c\,\frac{\delta(x+\Delta x) - \delta(x-\Delta x)}{2\Delta x} . \tag{26}$$

The form of the integral (25) allows yet another version of a Bessel generating function ([12], eq 9.1.43) to produce an exact formula for its weights

$$w_n^b(t) = -\frac{1}{2}\left(J_{2n-1}\left(\frac{2ct}{\Delta x}\right) + J_{2n+1}\left(\frac{2ct}{\Delta x}\right)\right) = -\frac{n\Delta x}{ct}\, J_{2n}\left(\frac{2ct}{\Delta x}\right) \tag{27}$$

[2]This is equivalent to the first-order system: $\partial u/\partial t + (c/\Delta x)(v(x+\Delta x,t) - v(x,t)) = 0$ and $\partial v/\partial t + (c/\Delta x)(u(x,t) - u(x-\Delta x,t)) = 0$ that mixes upwind and downwind differencing.

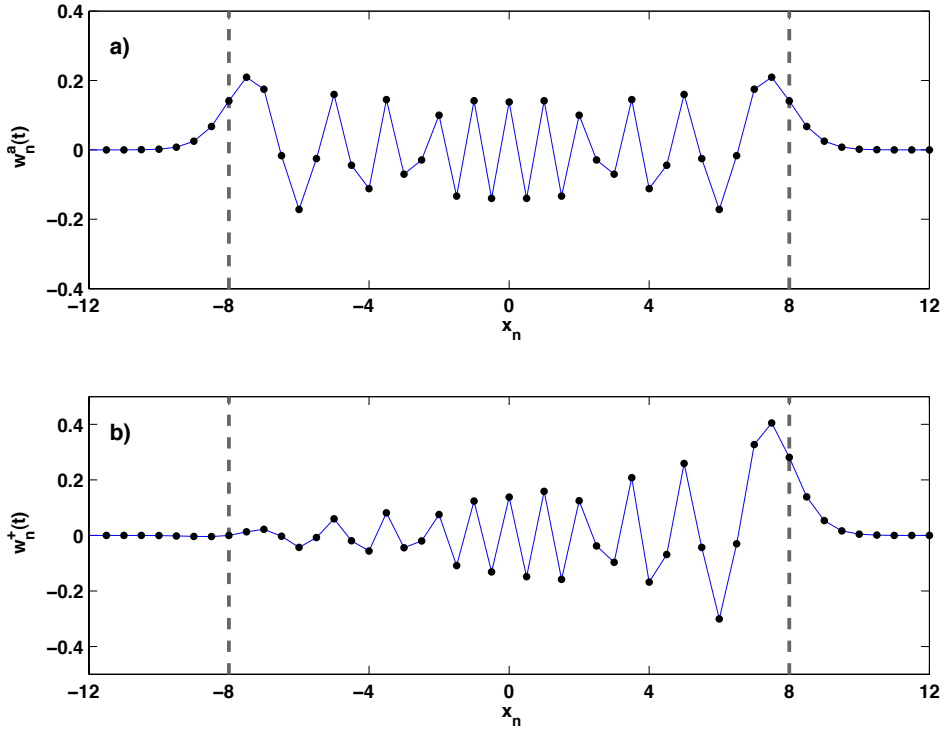

Figure 4: Two semi-discrete Green's functions for the wave equation for $\Delta x = 1/2$ at time $ct = 8$: a) bi-directional waves $w_n^1(n)$ and b) rightward waves $w_n^+(t)$. The gray dashed lines demarcate the group velocity region $|x| < ct$. The thin line serves only to connect the discrete values. The bi-directional Green's function consists of every second value of the one-way wave of Figure 1b.

where the final form follows from a Bessel recurrence relation ([12], eq 9.1.27). The derivative initial condition (26) is such that the linear combinations $\mathcal{W}^{\pm}(x,t) = \mathcal{W}^a(x,t) \pm \mathcal{W}^b(x,t)$ give, to within the centered-difference approximation, Green's functions for uni-directional propagation. The weights for the right-moving solution $w_n^+(t)$ are shown in Figure 4b, and now shows little trace of an Airy precursor at the trailing edge. It should be noted that this uni-directional solution includes Fourier modes of the so-called *parasitic* variety [2, 3]. Interestingly, the net result is a partial cancellation of the reverse propagation as it occurs in the purely one-way case.

3. An Analysis of Resolution Errors

The broad spatial extent of the numerical Green's function (5) is a direct illustration of the potential for dispersive errors due to under-resolution in the SD one-way wave (1). As suggested by the convolution (10) in Section 2, for centered-difference solutions to be well-resolved, it must be that contributions from the oscillatory tail of $\mathcal{G}(x,t)$ cancel in the integration due to relative smoothness in the initial condition $U(x)$. This is the crux of the resolution issue for the finite-difference approximation (1) [10].

We begin from the general solution for (1)

$$u(x,t) = \frac{1}{2\pi}\int_{-\infty}^{+\infty} \hat{U}(k)\, e^{ikx}\, e^{-i\omega(k)t}\, dk \tag{28}$$

where $\hat{U}(k)$ is the Fourier transform of the initial condition, and $\omega(k)$ is the SD dispersion relation (2). The standard approach for small Δx considers the cubic Taylor approximation of the discrete dispersion relation

$$\omega(k) \approx c\left\{(k\Delta x) - \frac{1}{6}(k\Delta x)^3\right\}\ . \tag{29}$$

Under this Taylor approximation, the Fourier integral becomes a solution to the modified equation [7]

$$u_t + c\,u_x + \left(\frac{c\Delta x^2}{6}\right) u_{xxx} = 0 \tag{30}$$

which provides a dynamical description of the numerical error by including the dispersive perturbative correction [4]. Furthermore, when $\hat{U}(k) \equiv 1$, the approximated integral is the Green's function of (30) and has the exact expression

$$u(x,t) = \left(\frac{2}{ct\Delta x^2}\right)^{1/3} \mathrm{Ai}\left(\left(\frac{2}{ct\Delta x^2}\right)^{1/3} (x - ct)\right) \tag{31}$$

which embodies the familiar explanation for the trailing oscillations. Upon the substitution $x_n = n\Delta x$ and the restriction to the leading edge $x_n/ct \sim 1$, the above recovers the discrete Airy precursor (8) up to the scaling of Δx that compensates for the delta function behavior.

3.1. Phase Analysis for a Gaussian Testcase

As an alternative approach to the characterization of the numerical error, in this section, the asymptotic method of steepest descent is applied to the Fourier integral solution for a Gaussian initial condition

$$U(x/a) = e^{-(x/a)^2} \quad ; \quad \hat{U}(ka) = a\sqrt{\pi}\, e^{-(ka/2)^2} \tag{32}$$

that incorporates a scale factor a. The Gaussian form has two simplifying advantages, the first being that the Fourier solution has the convenient exponential integrand

$$u(x,t) = \frac{a\sqrt{\pi}}{2\pi} \int_{-\infty}^{+\infty} e^{\phi(k)}\, dk \tag{33}$$

where $\phi(k)$ is the complex-analytic phase function

$$\phi(k) = ikx - i\,\frac{ct}{\Delta x}\,\sin k\Delta x - \left(\frac{ka}{2}\right)^2 . \tag{34}$$

The second feature of this Gaussian testcase is that the nondimensionalizations

$$\kappa = k\Delta x \quad ; \quad \epsilon = \frac{\Delta x}{a} \quad ; \quad X = \epsilon\,\frac{x}{a} \quad ; \quad T = \epsilon\,\frac{ct}{a} \tag{35}$$

permit the re-expression of the exponent in the form

$$\phi(k) = \frac{1}{\epsilon^2}\left\{i\kappa X - iT\,\sin\kappa - \frac{\kappa^2}{4}\right\} = \frac{1}{\epsilon^2}\,\Phi(\kappa)\,. \tag{36}$$

whose κ-space saddlepoint analysis is independent of the parameter ϵ that characterizes the numerical resolution. The steepest descent, and the stationary phase (or group velocity) methods are closely related asymptotic analyses for oscillatory integrals — but the latter allows for the analysis of more general complex-valued exponents [13]. Stationary phase analysis [8] is often justified in a long-time ($T \gg 1$) limit, and assumes a separation of scale between the wavescales and variations in the Fourier amplitude, $\hat{U}(k)$ [14]. The steepest descent perspective that follows offers a subtle advantage with the incorporation of the specific initial condition into the leading-order phase analysis.

3.2. A Resolution-Independent Map of Wave Error

Under the scalings (35), the limit of fine resolution $\epsilon = \Delta x/a \to 0$ is also the limit of rapid oscillation of the dimensionless integral solution

$$u(X,T) = \frac{1}{2\sqrt{\pi}} \int_S e^{\Phi(\kappa)/\epsilon^2}\, d\kappa \tag{37}$$

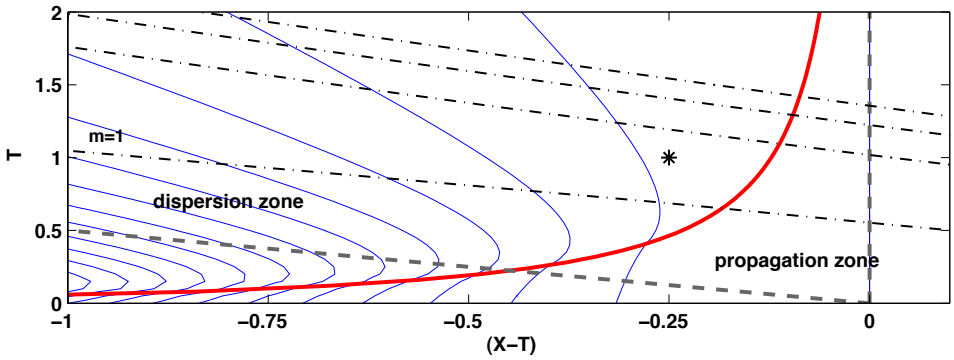

Figure 5: Space-time map ($X - T$ versus T) for the steepest descent analysis of the semi-discrete one-way wave (1) with a Gaussian initial condition. The thin, dark curves are negative-valued contours of the maximum value $\mathrm{Re}\{\Phi(\kappa_s)\}$ at intervals of 1/10 (T-axis is the zero contour), and are indicative of relative solution amplitude. The dashed, light lines demarcate the group velocity region $|X| < T$. The thick, dark curve represents the critical boundary (40) beyond which dispersive waves can appear. The light, dot-dashed curves indicate the onsets of the first four of the exponentially-small aliasing errors (first onset is labelled, $m = 1$).

so that the method of steepest descent applies [13]. The first step in the method is the deformation of the real-line integration path to follow instead a contour $\mathcal{S}$ along which the imaginary part of the complex phase is piecewise constant. The second step is to identify points along this contour which make asymptotically significant contributions to the integral. For the phase function (36), these are saddlepoints, $\kappa_s(X, T)$, which satisfy the stationarity condition

$$\Phi'(\kappa_s) = iX - iT\,\cos\kappa_s - \frac{\kappa_s}{2} = 0\,. \tag{38}$$

The local contribution to the integral near each saddlepoint, κ_s, is obtained by a quadratic Taylor approximation of the phase function $\Phi(\kappa)$, which is integrated to give

$$\frac{1}{2\sqrt{\pi}}\int_{\mathcal{S}_s} e^{\Phi(k)/\epsilon^2}\,dk \sim \frac{\epsilon}{\sqrt{2|\Phi''(\kappa_s)|}}\,e^{\Phi(\kappa_s)/\epsilon^2}\,. \tag{39}$$

The sum over all saddlepoints gives the steepest descent approximation to the solution $u(X, T)$ — the most significant contributions are distinguished by the saddlepoints at which the real part of $\Phi(\kappa_s)$ is largest.

Analysis of the saddlepoint condition (38) for (X, T) values results in the contour map (Figure 5) of the largest value of $\mathrm{Re}\{\Phi(\kappa_s)\}$. The travelling coordinate $X - T$ follows the rightward propagation so that the vertical (thick, gray dashed) line, and the line with slope -2 demarcate the (nondimensional) group velocity region $|X| < T$. The T-axis is a zero contour of $\mathrm{Re}\{\Phi(\kappa_s)\}$, with successive (thin, dark) contours at decreasing intervals of 1/10 that indicate the relative decay of solution amplitude. There are two clearly distinct regimes — these are labelled as the *propagation* and *dispersion zones*. For (X, T) values in the propagation zone, the largest value of $\mathrm{Re}\{\Phi(\kappa_s)\}$ is attained at a single saddlepoint located on the imaginary axis. In the dispersion zone, the largest value of $\mathrm{Re}\{\Phi(\kappa_s)\}$ is attained at two saddlepoints that symmetrically straddle the imaginary axis; and in this case, non-zero values of $\mathrm{Im}\{\Phi(\kappa_s)\}$ lead to oscillatory contributions from (39). The boundary between these zones is defined by the critical condition

$$\Phi''(\kappa_s) = iT\,\sin\kappa_s - \frac{1}{2} = 0 \tag{40}$$

and is plotted as the thick, dark curve in Figure 5. Within the dispersion zone, the downstream bending of the contours of maximum $\mathrm{Re}\{\Phi(\kappa_s)\}$ indicates the development of the trailing wavetrain. It should noted that (40) coincides with the turning-point failure [13] of the saddlepoint approximation, so that amplitude information from (39) is only asymptotically valid away from the zone boundary.

3.3. Threshold Time for the Visible Appearance of Waves

The resolution-independence of the steepest descent map implies a self-similarity property for the location of waves. However, the amplitude, and hence the visibility, of the waves is more strongly controlled by the exponential

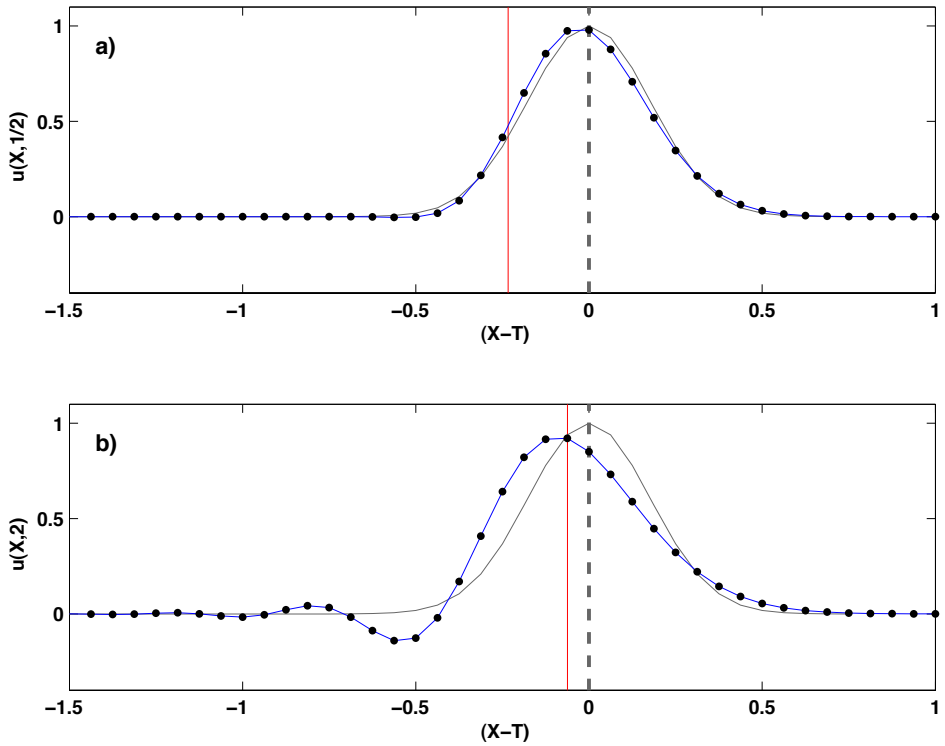

Figure 6: Semi-discrete solutions, $u(X,T)$, for the Gaussian resolution testcase shown in the travelling frame with $\epsilon = 1/4$ at two times: a) $T = 1/2$, and b) $T = 2$. The gridpoint values are exactly those obtained by convolutions (10) of an initial Gaussian ($a = 1$) with the discrete Green's functions of Figure 1. The thin connecting lines connect the discrete values of the computed solution (thin, dark) and the initial Gaussian (thin, light). The solid vertical divider indicates the boundary of the dispersion zone.

scaling in (39). In the nondimensionalization (35), the translating pulse roughly lies within $|X - T| < O(\epsilon)$. The zone boundary (40) can be shown to have the asymptotic form

$$T \sim -\frac{1}{8(X-T)} \tag{41}$$

in the large T limit. Combining these determines a scaling law for the times at which visible oscillations are predicted by steepest descent, $T \gg 1/8\epsilon$; or

$$t \gg \frac{a}{8\epsilon^2 c} \tag{42}$$

as is dimensionally consistent with (30). In Figure 6, computed SD solutions for $\epsilon = 1/4$ at times $T = 1/2$ and 2 are compared, in the travelling frame, to the initial Gaussian. These solutions, for Gaussian scale $a = 1$, coincide with the convolutions (10) using the Green's functions depicted in Figure 1. The top panel at $T = 1/2$ is just at the onset time of dispersive waves (42), and the solid vertical line shows the dispersive zone just encroaching on the Gaussian profile. At the later time $T = 2$, dispersive waves have become clearly visible in the dispersion zone.

3.4. Exponentially-Small Aliasing Errors

Asymptotic corrections beyond (39) can be determined by keeping cubic and higher terms in the Taylor expansion of the phase function $\Phi(\kappa)$ at saddlepoints κ_s. These errors (apparent in Figure 6a) constitute effects at algebraic powers of Δx, that can be analyzed through higher-order corrections to the modified equation analysis (30). However, this steepest descent perspective reveals yet another type of asymptotic error due to the appearance of additional saddlepoints at larger values of T. An example of this is shown by the steepest descent contour illustrated in Figure 7

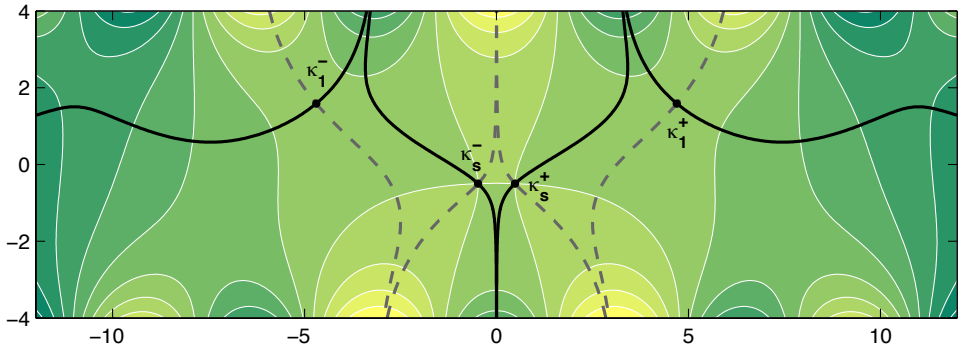

Figure 7: Steepest descent analysis of $\Phi(\kappa)$ in the complex κ-plane for $X = 1/4$, $T = 1$. The grayscale indicates level contours of $\mathrm{Re}\{\Phi(\kappa)\}$ (at intervals of 8). Thick contours (dark, solid and light, dashed) are steepest descent paths — piecewise curves along which $\mathrm{Im}\{\Phi(\kappa)\}$ is constant. The integration path (dark contour) includes four saddlepoint contributions. The largest contributions to the integral (37) are due to the saddlepoints labelled $\kappa_s^{\pm}$. Exponentially-smaller aliasing errors are due to $\kappa_1^{\pm}$. The (X, T) values for this analysis correspond to the $*$ marked on the steepest descent map (5).

for $(X, T) = (1/4, 1)$, where the integration path (dark, solid contour) includes four saddlepoint contributions. By the contouring of $\mathrm{Re}\{\Phi(\kappa)\}$, it is seen that relative to the dominant saddlepoints ($\kappa_s^{\pm}$), these additional saddlepoints ($\kappa_1^{\pm}$) are exponentially smaller in ϵ. Hence, these errors are asymptotically less significant than all of the algebraic errors local to the saddlepoints κ_s. At larger T, it is found that the steepest descent contour passes through a sequence of such saddlepoints ($\kappa_m^{\pm}$) The first four thresholds for the participation of these additional saddlepoints are shown in Figure 5 as thin, dash-dot curves, with the first threshold labelled as $m = 1$. The values $(X, T) = (1/4, 1)$ correspond to the $*$ marked on the steepest descent map (5) within the region having one additional pair of saddlepoints. The origin of these saddlepoints is rooted in the periodicity of the group velocity $\omega'(k)$, and are seemingly related to the aliasing errors envisioned in [15] and [8]. Finally, since the Green's function also represents the long-time evolution of a localized initial condition [14], it is by the emergence of these additional saddlepoints that the incoherent waves of the SD Green's function (6) is achieved in the $T \to \infty$ limit.

3.5. Fully-Discrete Leapfrog Scheme for the One-Way Wave Equation

In this section, the highlights for a steepest descent analysis for a fully-discrete scheme, second-order leapfrog (LF), are presented. Consider then, the LF discretization of the one-way wave equation

$$\frac{u(x, t + \Delta t) - u(x, t - \Delta t)}{2\Delta t} + c\, \frac{u(x + \Delta x, t) - u(x - \Delta x, t)}{2\Delta x} = 0\,. \tag{43}$$

Upon reflection, the Fourier integral

$$u(x, t) = \frac{1}{2\pi} \int_{-\infty}^{+\infty} \hat{U}(k)\, e^{ikx}\, \exp\left(-\frac{it}{\Delta t} \sin^{-1}\left\{ \frac{c\Delta t}{\Delta x}\, \sin k\Delta x \right\} \right) dk \tag{44}$$

that is obtained using the LF dispersion relation, while defined for continuous values of x and t, is also an exact solution to the LF discretization (43) for the initial value $u(x, 0) = U(x)$. Only the case of CFL number, $C \equiv c\Delta t/\Delta x$, in the stable range of $0 \le C \le 1$ is considered here. In the above integral representation of the solution, it is assumed that the inverse branch has $\sin^{-1} 0 = 0$ and is continuous for the real-k path of integration. This particular branch choice means that this solution is perfectly constructed to be devoid of parasitic waves [3].

Using the nondimensionalization (35), the Gaussian resolution testcase gives the ϵ-independent LF phase function

$$\Phi(\kappa) = i\kappa X - iT\, \frac{\sin^{-1}(C \sin \kappa)}{C} - \frac{\kappa^2}{4}\,. \tag{45}$$

The only significant difference in the complex analysis for this LF case is the appearance of branch points, κ_b, occurring where $\sin \kappa_b = 1/C$. But again, a steepest descent map results from the identification of points in the X-T plane

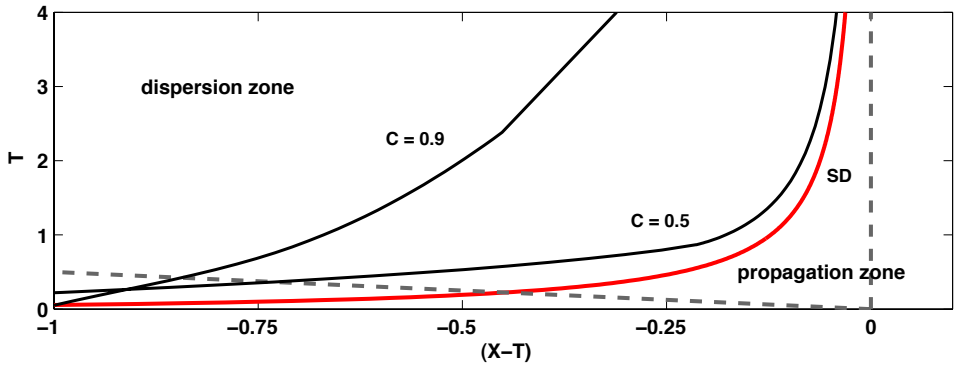

Figure 8: Space-time map ($X - T$ versus T) for the steepest descent analysis of the leapfrog scheme for the one-way wave (43) with a Gaussian initial condition. The thick, dark curves show the boundary between regions where the steepest descent approximation (non-parasitic solution) is dominated by a single saddle point (non-oscillatory), and a pair of saddlepoints (oscillatory). Two values of CFL number $C = 0.5$ and 0.9 are compared with the SD region ($C = 0$) from Figure 5. The dashed, light lines demarcate the group velocity region $|X| < T$.

where the largest contribution is due to a saddlepoint on the imaginary axis, or a pair of saddlepoints symmetric across the imaginary axis. Figure 8 illustrates the migration of the boundary between the propagation and dispersion zones as the CFL number increases from the SD value of $C = 0$. The deferral of visible waves as C increases towards one is evident in the widening of the propagation zone; and a long-time asymptotic analysis verifies that the threshold time for visible waves, relative to (42), is lengthened by a factor of $1/(1-C^2)$. It can be shown that the LF scheme can admit aliasing-type errors as described earlier — these can arise not only to saddlepoints, but also from the branchpoints in the complex analysis.

4. In Closing

As theoretical background, the SD approximation has also served as a point of reference for computations of the Hamilton-Jacobi equations [16], and the Helmholtz problems [17, 18]. For the inviscid Burgers equation, the SD approximation, has the deeper property of exact integrability [19], and continues to drive further theory in nonlinear waves [20]. Although inherently one-dimensional analyses, the results presented here reveal a mathematical complexity that does not readily generalize, yet reveal canonical features of dispersion errors and provide a framework for interpretation in more general settings. Even the with the aliasing errors of Section 3.4, one could imagine such effects becoming much more significant with nonlinearity and less smooth solutions.

In the demand for scientific understanding, computational models are pushed to their very limits of performance. In computational fluid dynamics, there are many instances where waves are subject to marginal resolution. For instance, atmospheric weather and climate models quite often develop significant features at near-resolution scales that can have associated wave errors [22, 23]. While waves such as these may be unintended numerical artifacts, they are often observable in the model outputs, and their dynamics should be understood for what they are. Expository in nature, these results are presented for their alternative perspective on the foundational ideas underlying the numerical computation of wave equations.

Acknowledgments

The author acknowledges support from NSERC RGPIN-238928.

References

[1] V. Thomée, *From finite differences to finite elements: A short history of numerical analysis of partial differential equations*, Journal of Computational and Applied Mathematics, 128 (2001), pp. 1–54.

[2] D.R. Durran, *Numerical Methods for Wave Equations in Geophysical Fluid Dynamics*, Springer, New York (1999) 465pp.
[3] J. Strikwerda, *Finite Difference Schemes and Partial Differential Equations*, SIAM, Philadelphia, (2004), 450pp.
[4] R.J. Leveque, *Finite Difference Methods for Ordinary and Partial Differential Equations*, SIAM, Philadelphia, (2007), 341pp.
[5] K.W. Morton & D.F. Meyers, *Numerical Solutions of Partial Differential Equations*, Cambridge Univ. Press, (2004), 227pp.
[6] A. Iserles, *A First Course in the Numerical Analysis of Differential Equations*, Cambridge Univ. Press, (1996), 378pp.
[7] R.F. Warming & B.J. Hyett, *The Modified Equation Approach to the Stability and Accuracy Analysis of Finite-Difference Methods*, J. Comput. Phys. 14 (1974), pp. 159179.
[8] L.N. Trefethen, *Group Velocity in Finite Difference Schemes*, SIAM Review, 24 (1982), pp. 113–136.
[9] C.E. Pearson, *Asymptotic Behavior of Solutions to the Finite-Difference Wave Equation*, Mathematics of Computation, 23 (1969), pp. 711–715.
[10] C.E. Pearson, *Upwind and Downwind Effects of Numerical Approximations to Wave Equations*, Communications in Applied Numerical Methods, 4 (1988), pp. 517–520.
[11] R. Vichnevetsky & J.B. Bowles, *Fourier Analysis of Numerical Approximations of Hyperbolic Equations*, SIAM, Philadelphia, (1982), 140pp.
[12] Abramowitz & I. Stegun, *Handbook of Mathmatical Functions*, National Bureau of Standards, Washington DC (1964).
[13] C. Bender & S.A. Orszag, *Advanced Mathematical Methods for Scientists and Engineers*, McGraw-Hill, New York (1978), 465pp.
[14] G.B. Whitham, *Linear and Nonlinear Waves*, Wiley, New York (1974) 635pp.
[15] W.L. Briggs & T. Sarie, *Finite Difference Solutions of Dispersive Partial Differential Equations*, Mathematics and Computers in Simulation, XXV (1983), pp. 268–278.
[16] S. Bryson & D. Levy, *High-order semi-discrete central-upwind schemes for multi-dimensional Hamilton–Jacobi equations*, Journal of Computational Physics, 189 (2003), pp 63-87.
[17] A. Zemla, *On the fundamental solutions for the difference Helmholtz operator*, SIAM Journal on Numerical Analysis, 32 (1995), pp 560-570.
[18] H.S. Bhat & B. Osting, *Diffraction on the Two-Dimensional Square Lattice*, SIAM J. Appl. Math., 70 (2009), pp 1389-1406.
[19] J. Goodman & P.D. Lax, *On dispersive difference schemes I*, Comm. Pure Appl. Math., 41 (1988), pp. 1-25.
[20] B. Hayes, *Binary modulated oscillations in a semi-discrete version of Burgers equation*, Physica D, 106 (1997), pp 287-313.
[21] T. Hou & P.D. Lax, *Dispersive Approximations in Fluid Dynamics* Comm. Pure Appl. Math., 44 (1991), pp. 1-10.
[22] R. Grotjahn *Group Velocity Errors Caused by Finite-Differencing: a Meteorological Perspective*, Mathematics and Computers in Simulation, 27 (1985), pp. 37–46.
[23] M.A. Geller, et.al., *Gravity Waves Issues & Challenges for the Community*, The Institute for Integrative and Multi-disciplinary Earth Studies, White paper (2006), 19pp.